

# Fluid-flow-induced flutter of a flag

Médéric Argentina and L. Mahadevan<sup>a</sup>

Division of Engineering and Applied Sciences, Harvard University, Pierce Hall, 29 Oxford Street, Cambridge, MA 02138

Communicated by Joseph B. Keller, Stanford University, Stanford, CA, November 16, 2004 (received for review February 20, 2004)

**We give an explanation for the onset of fluid-flow-induced flutter in a flag. Our theory accounts for the various physical mechanisms at work: the finite length and the small but finite bending stiffness of the flag, the unsteadiness of the flow, the added mass effect, and vortex shedding from the trailing edge. Our analysis allows us to predict a critical speed for the onset of flapping as well as the frequency of flapping. We find that in a particular limit corresponding to a low-density fluid flowing over a soft high-density flag, the flapping instability is akin to a resonance between the mode of oscillation of a rigid pivoted airfoil in a flow and a hinged-free elastic plate vibrating in its lowest mode.**

The flutter of a flag in a gentle breeze and the flapping of a sail in a rough wind are commonplace and familiar observations of a rich class of problems involving the interaction of fluids and structures, of wide interest and importance in science and engineering (1). Folklore attributes this instability to some combination of (i) the Bénard–von Kármán vortex street that is shed from the trailing edge of the flag and (ii) the Kelvin–Helmholtz problem of the growth of perturbations at an interface between two inviscid fluids of infinite extent moving with different velocities (2). However, a moment's reflection makes one realize that neither of these is correct. The frequency of vortex shedding from a thin flag (with an audible acoustic signature) is much higher than that of the observed flapping, while the lack of a differential velocity profile across the flag and its finite flexibility and length make it qualitatively different from the Kelvin–Helmholtz problem. After the advent of high-speed flight, these questions were revisited in the context of aerodynamically induced wing flutter by Theodorsen (3–5). While this important advance made it possible to predict the onset of flutter for rigid plates, these analyses are not directly applicable to the case of a spatially extended elastic system such as a flapping flag. Recently, experiments on an elastic filament flapping in a flowing soap film (6) and of paper sheets flapping in a breeze (ref. 7 and references therein) have been used to further elucidate aspects of the phenomena such as the inherent bistability of the flapping and stationary states, and a characterization of the transition curve. In addition, numerical solutions of the inviscid hydrodynamic (Euler) equations using an integral equation approach (8) and of the viscous (Navier–Stokes) equations (9) have shown that it is possible to simulate the flapping instability. However, the physical mechanisms underlying the instability remain elusive. In this paper, we remedy this in terms of the following picture: For a given flag, there is a critical flow velocity above which the fluid pressure can excite a resonant bending instability, causing it to flutter. In fact, we show that in the limit of a heavy flag in a fast-moving light fluid the instability occurs when the frequency associated with the lowest mode of elastic bending vibrations of the flag becomes equal to the frequency of aerodynamic oscillations of a hinged rigid plate immersed in a flow.

Physically, the meaning of this result is as follows: For a heavy flag in a rapid flow, the added mass effect due to fluid motion is negligible so that the primary effect of the fluid is an inertial pressure forcing on the plate. For a plate of length  $L$  weakly tilted at an angle  $\theta$ , the excess fluid pressure on it scales as  $\rho_f U^2 \theta$ , where  $\rho_f$  is the fluid density and  $U$  is the fluid velocity. The inertia of a plate of thickness  $h$ , of density  $\rho_s$ , and oscillating at a frequency

$\omega_a$  scales as  $\rho_s h \omega_a^2 L \theta$ . Equating the two yields the frequency of oscillations of a freely hinged rigid plate approximately parallel to the flow  $\omega_a \sim (\rho_f U^2 / \rho_s h L)^{1/2}$ . On the other hand, for a flexible plate of thickness  $h$  and made of a material of Young's modulus  $E$  (bending stiffness of order  $Eh^3$ ) the elastic restoring force per unit length due to a deflection by the same angle  $\theta$  scales as  $Eh^3 \theta / L^3$  so that the frequency of the lowest mode of free bending vibrations of a flexible plate  $\omega_b \sim (Eh^2 / \rho_s L^4)^{1/2}$ . Equating the two yields a critical velocity for the onset of flutter of a plate of given length  $U_c \sim (Eh^3 / \rho_f L^3)^{1/2}$ . As we will see in the following sections, this simple result arises naturally from the analysis of the governing equations of motion of the flag and the fluid. In particular, our analysis is capable of accounting for the unsteady nature of the problem in terms of the added mass of the fluid and the vortex shedding from the trailing edge in terms of the seminal ideas of Theodorsen (3).

## Equations of Motion

**Elasticity.** We consider the dynamics of an inextensible two-dimensional elastic plate<sup>b</sup> of length  $L$ , width  $l$ , and thickness  $h \ll L \ll l$ , made of a material of density  $\rho_s$  and Young's modulus  $E$  embedded in a three-dimensional parallel flow of an ambient fluid with a density  $\rho_f$  and kinematic viscosity  $\nu$ , shown schematically in Fig. 1. We assume that the leading edge of the naturally straight plate is clamped at the origin with its tangent along the  $x$  axis and that there are no variations in the flow along the direction of the clamped edge, and that far from the plate, the fluid velocity  $\mathbf{U} = U\mathbf{x}$ . Then the transverse position of the plate  $Y(x, t)$  satisfies the equation of motion (10):

$$mY_{tt} = -BY_{xxxx} + l\Delta P + TY_{xx}. \quad [1]$$

Here, and elsewhere  $A_b \equiv \partial A / \partial b$ ,  $m = \rho_s h l$  is the mass per unit length of the flag,  $B = Eh^3 l / 12(1 - \sigma^2)$  is its flexural rigidity (here  $\sigma$  is the Poisson ratio of the material),  $\Delta P$  is the pressure difference across the plate due to fluid flow, and  $T$  is the tension in the flag induced by the flow.

In deriving Eq. 1, we have assumed that the slope of the plate is small so that we can neglect the effect of any geometrical nonlinearities; these become important in determining the detailed evolution of the instability but are not relevant in understanding the onset of flutter. For the case when the leading edge of the flag is clamped and the trailing edge is free, the boundary conditions associated with Eq. 1 are (10):

$$\begin{aligned} Y(t, 0) = 0, \quad Y_x(t, 0) = 0, \\ Y_{xx}(t, L) = 0, \quad Y_{xxx}(t, L) = 0. \end{aligned} \quad [2]$$

To close the system of Eqs. 1 and 2, we must evaluate the fluid pressure  $\Delta P$  by solving the equations of motion for the fluid in the presence of the moving plate.

<sup>a</sup>To whom correspondence should be addressed. E-mail: lm@deas.harvard.edu.

<sup>b</sup>Our analysis also carries over to the case of an elastic filament in a two-dimensional parallel flow.

© 2005 by The National Academy of Sciences of the USA



$$C[\gamma] = \int_1^\infty \frac{x_0}{\sqrt{x_0^2 - 1}} \gamma dx_0 / \int_1^\infty \sqrt{\frac{x_0 + 1}{x_0 - 1}} \gamma dx_0 \quad [10]$$

is the Theodorsen functional (3) quantifying the unsteadiness of the flow. For example, for an airfoil at rest that starts to move suddenly at velocity  $U$ ,  $\gamma = \delta(x_0 - (2/L) Ut)$  corresponding to the generation of lift due to a vortex that is shed and advected with the fluid. Then

$$C = 1 - \frac{L}{2Ut}. \quad [11]$$

We see that as  $Ut/L \rightarrow \infty$ ,  $C \rightarrow 1$ , which limit corresponds to the realization of the Kutta condition for steady flow (12). Adding up the contributions to the pressure jump across the plate from the circulatory and noncirculatory flows given by Eqs. 5 and 9 we have  $\Delta P = P_{nc} + P_\gamma$ , i.e.,

$$\Delta P = -\rho_f U C[\gamma] f\left(\frac{x}{L}\right) (Y_t + UY_x) - L \rho_f n\left(\frac{x}{L}\right) Y_{tt}, \quad [12]$$

where the dimensionless functions  $n(s)$  and  $f(s)$  are

$$f(s) = 2 \sqrt{\frac{1-s}{s}}, \quad [13]$$

$$n(s) = 2 \sqrt{(1-s)s}. \quad [14]$$

By way of comparison, our consideration of the fluid forces embodied in Eq. 12 differs from that of Crighton and Oswell (13), who treated the case of an infinite plate avoiding many of the complications of a finite plate, and is also different from the treatment of Fitt and Pope (8), who neglected the role of fluid added-mass. In the slightly different context of fish swimming, Lighthill (14) considered an undulating slender body such as an eel swimming at high Reynolds number for which he wrote

$$\Delta P = (\partial_t + U\partial_x)(a(x)v),$$

for the lateral force exerted by the fish on a water slice by equating it to the material derivative of the momentum liberated in the fluid, with  $a(x)$  as an ad hoc representation of the apparent mass of the cross section at  $x$ , and  $v = Y_t + UY_x$ . Our theory differs from this by explicitly accounting for the potential flow field and vortex shedding using the Theodorsen approach in the limit of small deformations when the vertical velocity  $v$  is almost constant, and suggests an obvious extension of our work to locomotion.

**Aeroelasticity.** Substituting Eq. 12 in Eq. 1 (with  $T = 0$ ) gives us a single equation of motion for the hydrodynamically driven plate

$$\begin{aligned} mY_{tt} &= -BY_{xxxx} \\ &\quad -\rho_f U C[\gamma] f\left(\frac{x}{L}\right) (Y_t + UY_x) \\ &\quad -L \rho_f n\left(\frac{x}{L}\right) Y_{tt}, \end{aligned} \quad [15]$$

with  $C[\gamma]$  determined by Eq. 10. We note that Eq. 15 accounts for the effects of unsteady flow past a flexible plate of finite length, including vortex shedding and fluid added-mass, but is only valid for small-amplitude motions. To make Eq. 15 dimensionless, we scale all lengths with the length  $L$  of the flag, so that

$x = sL$ ,  $Y = \eta L$ , and scale time with the bending time  $L/U_B$ , where  $U_B = (1/L)\sqrt{(B/m)}$  is the velocity of bending waves of wavelength  $2\pi L$ . Then Eq. 15 may be written as

$$\mathcal{M}\eta_{\tau\tau} = -\eta_{ssss} - \rho u_0 C[\gamma] f(s) (\eta_\tau + u_0 \eta_s). \quad [16]$$

Here  $\mathcal{M} = 1 + \rho n(s)$ , where  $\rho = (l\rho_f L/m) = (\rho_f/\rho_s)(L/h)$  characterizes the added mass effect and the parameter  $u_0 = (U/U_B)$  is the ratio of the fluid velocity to the bending wave velocity in the plate. We can use symmetry arguments to justify the aerodynamic pressure  $C[\gamma]f(s)(\eta_\tau + u_0\eta_s)$ : the term  $\eta_s$  arises because the moving fluid breaks the  $s \rightarrow -s$  symmetry, while the term  $\eta_\tau$  arises because the plate exchanges momentum with the fluid, so that the time reversibility  $\tau \rightarrow -\tau$  symmetry is also broken. These two leading terms in the pressure, which could have been written down on grounds of symmetry, correspond to a lift force proportional to  $\eta_s$  and a frictional damping proportional to  $\eta_\tau$ . By considering the detailed physical mechanisms, we find that the actual form of these terms is more complicated due to the inhomogeneous dimensionless functions  $f(s)$ ,  $n(s)$ . Thus, understanding the flapping instability reduces to a stability analysis of the trivial solution  $\eta = 0$  of the system 16, 2 to perturbations as a function of the problem parameters  $\rho$ ,  $u_0$ .

Since the free vortex sheet is advected with the flow, the vorticity distribution may be written as  $\gamma = \gamma((2U/L)(t - t_1) - x_0)$  and  $t_1$  being the time at which shedding occurs, which in dimensionless terms reads  $\gamma = \gamma(2u_0(\tau - \tau_1) - x_0)$ . Accounting for the oscillatory nature of the flapping instability with an unknown frequency  $\omega$  suggests that an equivalent description of the vorticity distribution is given by  $\gamma = Re(Ae^{i(\omega(\tau - \tau_1) - qx_0)})$ , where  $q = \omega/2u_0$  is a nondimensional wave number of the vortex sheet. Using the above traveling wave form of the vorticity distribution in Eq. 10 we get an expression for the Theodorsen function (3),

$$C[\gamma] = C(q) = \frac{H_1(q)}{H_0(q) + iH_1(q)}, \quad [17]$$

where  $H_i$  are Hankel functions of  $i$ th order. The system 16, 17, 2 completes the formulation of the problem for the stability of a straight flag.

### Stability Analysis

To understand the mechanism of instability of the trivial solution of 16, 2, we note that for a typical textile flag in fast-moving air, the added-mass parameter  $\rho \leq 1$ , while the scaled velocity  $u_0 \gg 1$ . We can thus simplify Eq. 16 even further by looking at the asymptotic limit  $\rho \rightarrow 0$ ,  $u_0 \rightarrow \infty$  but with the scaled aerodynamic pressure  $\rho u_0^2$  being finite. Furthermore, in this limit the vorticity is advected rapidly from the trailing edge so that we can use the quasi-steady approximation (15). This supposes that the lift forces are slaved adiabatically to those on a stationary airfoil with the given instantaneous transverse velocity  $Y_t + UY_x$ , so that  $C \rightarrow 1$ , following Eq. 11. By assuming that the Kutta condition is satisfied instantaneously, we overestimate the lift forces and thus expect to get a threshold for stability that is slightly lower than if  $C \neq 1$ . Then Eq. 16 becomes time-reversible:<sup>h</sup>

$$\eta_{\tau\tau} = -\eta_{ssss} - \rho u_0^2 f(s) \eta_s. \quad [18]$$

The two terms on the right-hand side of Eq. 18 correspond to the existence of two different modes of oscillation: (i) that of a flexible plate bending with a frequency that is dependent on the

<sup>h</sup>This is because the term breaking time reversal symmetry  $\rho u_0 \eta_\tau$  becomes negligibly small.

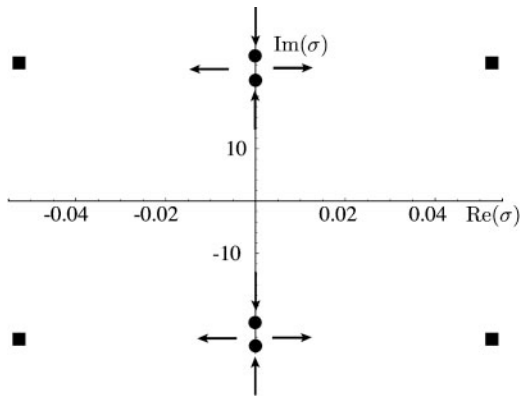


**Fig. 2.** Spectrum  $Im(\sigma)$ ,  $Re(\sigma)$  of the system (18,2) when  $\rho \ll 1$  (with  $u_0^* = (10.53/\sqrt{\rho})$ ). The eigenvalues with the smallest absolute value are plotted for  $u_0 = 0.9u_0^*$  (disks) and for  $u_0 = 1.1u_0^*$  (square). We see that instability occurs via a collision and splitting of two pairs of eigenvalues along the imaginary axis (indicated by the arrows) and is a signature of a 1:1 resonance mechanism in a time-reversible system.

wavenumber and (ii) that of a rigid plate in the presence of flow-aligning aerodynamic forces. In this limiting case, we can clearly see the physical mechanisms at work in determining the stability or instability of the plate: Small plates are very stiff in bending, but as the plate length becomes large enough for the fluid pressure to excite a resonant bending instability, the plate starts to flutter. Equivalently, the instability is observed when the bending oscillation frequency become of the order of the frequency of oscillations of a hinged rigid plate immersed in a flow. This simple picture allows us to estimate the criterion for instability by balancing the bending forces ( $Eh^3\eta/L^4$ ) with the aerodynamic forces  $\rho_f U^2(\eta/L)$  so that for a given flow field the critical velocity of the fluid above which the flag will flutter scales as

$$U_c \sim \left( \frac{Eh^3}{\rho_f L^3} \right)^{1/2}, \quad [19]$$

which in dimensionless terms corresponds to  $u_0 \sim 1/\rho^{1/2}$ . Then the typical flapping frequency  $\omega$  is given by balancing plate inertia  $\rho_s h \omega^2 \eta$  with the aerodynamic forces  $\rho_f U^2(\eta/L)$  and leads to

$$\omega \sim \left( \frac{\rho_f U^2}{\rho_s h L} \right)^{1/2}. \quad [20]$$

To see this quantitatively, we look for solutions to **18, 2** of the form  $\eta(s, \tau) = \xi(s)e^{\sigma\tau}$  and compute the associated spectrum,  $\sigma(u_0)$  using AUTO (16). In Fig. 2, we show that for  $u_0 < u_0^* = 10.53/\sqrt{\rho}$  with  $\rho \ll 1$ , the spectrum lies on the imaginary axis as expected, and as  $u_0 \geq u_0^*$ , the four eigenvalues with smallest absolute value collide and split, leading to an instability via a 1:1 resonance (17).

As  $\rho \sim O(1)$ , the effective damping term,  $\rho u_0 C f(s) \eta_\tau$ , becomes important, so that the spectrum is shifted to the left, i.e.,  $Re(\sigma) < 0$ . In this case, although the instability is not directly related to a resonance, the physical mechanism remains the same, i.e., a competition between the destabilizing influence of part of the fluid inertia and the stabilizing influence of elastic bending, subject to an effective damping due to fluid motion. Substituting the separable form  $\eta(s, \tau) = \xi(s)e^{\sigma\tau}$  into Eq. **16** we get

$$\sigma^2 \mathcal{M} \xi = -\xi_{ssss} - C[\gamma] \rho u_0 f(s) (\sigma \xi + u_0 \xi_s). \quad [21]$$

At the onset of the oscillatory instability,  $Re(\sigma) = 0$ , so that  $\sigma = i\omega$  and  $C[\gamma]$  is given by Eq. **17**. Together with the boundary conditions **2**, this yields a nonlinear eigenvalue problem for  $\omega$ ,  $\xi$  since the Theodorsen function  $C(q) = C(\omega/2u_0)$  depends on  $\omega$ . We again solve the resulting system numerically with the AUTO package (16), using a continuation scheme in  $\omega$  starting with a guess for the Theodorsen function  $C(\omega/2u_0) = C(0) = 1$ . The results, shown in Fig. 3, show that when  $u_0 > u_0^*(\rho)$ ,  $Re(\sigma) > 0$  with  $Im(\sigma) \neq 0$ , i.e., an oscillatory instability leading to flutter arises. We see that for sufficiently large  $u_0$ , the plate is always unstable, i.e., large enough fluid velocities will always destabilize the elastic plate. As  $\rho \gg 1$ , the added mass effect becomes relatively more important and it is easier for the higher modes of the plate to be excited. We note that the stability boundary when  $C \neq 1$  accounting for vortex shedding corresponds to a higher value of the scaled fluid velocity  $u_0$  than that obtained by using the quasi-steady approximation  $C = 1$ , and is a consequence of the quasi-steady approximation, which overestimates the lift forces. In Fig. 3 *Inset*, we see that as  $\rho \rightarrow 0$ ,  $q \rightarrow 0$ . Therefore,  $C(q) = C(0) = 1$  so that in this limit the quasi-steady hypothesis is a good approximation. In Fig. 4 we show the mode shapes when  $\rho < 1$  and  $\rho \gg 1$ ; as expected, the most unstable mode for  $\rho \gg 1$  is not the fundamental mode of the plate. We also see that the normalized amplitude of the unstable modes is maximal at the trailing edge; this is a consequence of the inhomogeneous functions  $f(s)$ ,  $n(s)$  in Eq. **16** as well as the clamped leading edge and a free trailing edge.

In Fig. 2 we also show the experimental transition curve obtained from a recent study on the onset of flutter in paper sheets (7). The large error bars in the experimental data are due to the fact that there is a region of bistability wherein both the straight and the flapping sheet are stable. Nevertheless, we see that we do capture the qualitative trends of the experiments, and in the following discussion we show that it is possible to do

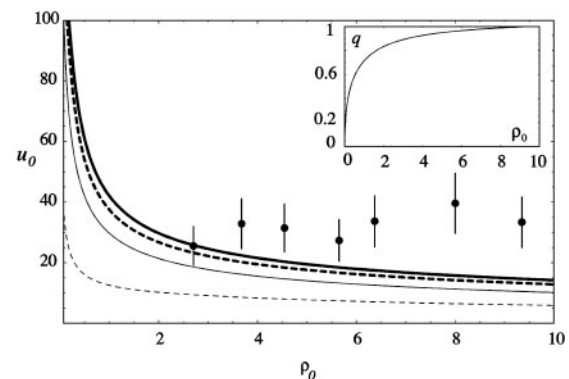


**Fig. 3.** Stability diagram obtained by solving the eigenvalue problem **16, 2** parametrized in terms of the scaled added mass,  $\rho$ , and the scaled flow velocity,  $u_0$ . The thin dashed line represents the transition curve using the quasi-steady approximation where  $C = 1$ ; for values of  $\rho$ ,  $u_0$  below this line, the flag is stable, and for values above it, it is unstable. The thin solid line represents the transition curve when vortex shedding is taken into account, i.e.,  $C \neq 1$ . The role of the third dimension and flag tension is considered in the appendices and changes the marginal stability curve slightly. The bold solid line is obtained by including three-dimensional effects using a simple model (see *Appendix 1*) for a flag of aspect ratio  $r = 2.5$ , and the bold dashed solid line takes into account the tension in the flag that arises due to viscous effects via a simple estimate of the Blasius boundary layer (see *Appendix 2*) with  $Re = 10^4$ . The dots correspond to experimental data characterizing the transition to flutter in three-dimensional flows past flexible sheets of paper (7); the large error bars are a consequence of the variations due to three-dimensional effects as well as regions of bistability where both the flapping and stationary state are stable. (*Inset*) The dimensionless wavenumber of the instability  $q = (\omega/2u_0)$  as a function of  $\rho$ . When  $\rho \ll 1$ ,  $q$  tends to be zero and  $C(q) \rightarrow 1$ .

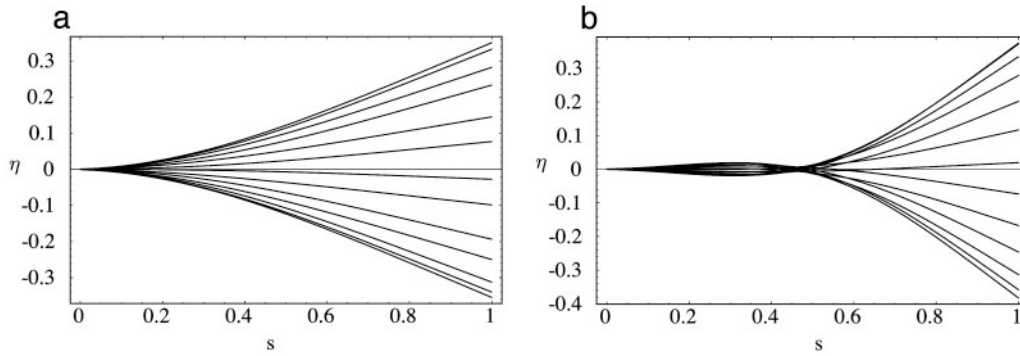


**Fig. 4.** Snapshots corresponding to the mode of instability  $\xi(s)$  with  $\rho = 0.2$ ,  $u_0 \approx 66$  (a) and  $\rho = 25$ ,  $u_0 \approx 6.6$  (b). We see that for sufficiently large values of the added mass parameter  $\rho$ , the primary instability of the flag flutter occurs in a higher mode than otherwise.

slightly better quantitatively by accounting for the effects of the tension in the flag due to viscous boundary layers and the third dimension.

### Discussion

Our linearized theory cannot capture the bistability in the transition to flutter without accounting for the various possible nonlinearities in the system arising from geometry. But even without accounting for these nonlinearities, there is a systematic discrepancy between our theory and the data, which consistently show a higher value of  $u_0$  for the onset of the instability. While there are a number of possible reasons for this, we believe that there are three likely candidates: The role of nonlocal interactions, three-dimensional effects, and the tension in the plate induced by the Blasius boundary layer, all of which would tend to stabilize the sheet and thus push the onset to higher values of  $u_0$ . Postponing the question of nonlocal interactions to the future, in *Appendix 1* we describe a simple model to account for three-dimensional effects and show that it pushes up the stability boundary as shown in Fig. 2. An explanation of this effect follows immediately from the fact that the added-mass parameter is rescaled due to the effects of the lateral boundaries of the flag. In *Appendix 2*, we consider the role of the tension in the flag due to the fluid induced shear at large but finite Reynolds numbers. Using the Blasius boundary layer calculation to determine the tension,  $T$ , via (I.1) a reworking of the stability analysis in the previous section pushes up the marginal stability curve by  $\approx 20\%$  when  $Re \sim 10^4$ , making the comparison with the experimental data quantitatively better. A final remark concerns the role of the free vortex sheet behind the flag. We have assumed that this sheet is localized to the vicinity of  $y = 0$ , but experimental observations (6, 7) show that a Kelvin–Helmholtz-like instability destabilizes the sheet giving it a transverse velocity component. Thus, the vortex sheet is advected at a velocity slower than that of the fluid. Neglecting the transverse dynamics of the vortex sheet as done here overestimates the lift forces and lowers the marginal stability curve for the onset of the instability.

The commonplace occurrence of flutter in a flag belies the complexity hidden in this phenomenon. Extracting a qualitative and quantitative understanding involves the consideration of a number of effects. Our hierarchy of models starting with a relatively simple physical picture of the basic resonance-like behavior to the more sophisticated analyses in the quasi-steady and the unsteady cases have allowed us to dissect the physical mechanisms involved. In particular, we account for the finite length and finite bending stiffness of the sheet, as well as the fluid effects due to added-mass, vortex shedding, three-dimensional flow, and viscous boundary layer drag. We also provide a relatively simple criteria for the onset of the instability in terms of the scaling laws (19, 20). There are clear avenues for

further questions, the most prominent of which include a detailed comparison with a two-dimensional numerical simulation and further experiments; these will be reported elsewhere.

### Appendix 1: Three-Dimensional Effects

In this appendix, we introduce an approach that accounts for three-dimensional effects. By introducing the noncirculatory velocity potential (Eq. 3), the flag is assumed to a flag of infinite span moving in the  $y$  direction with a velocity  $v$ . As a consequence,  $\phi_{nc}$  did not depend on the  $z$  variable. To generalize the analysis of Theodorsen to the case when the flag has finite width, we assume the flag to be a rectangular plate of length  $L$  and width  $l$ . Integrating the equation of motion for the plate (Eq. 1) in the  $z$  direction to simplify the problem in this case yields

$$\rho_s h l Y_{tt} = -B Y_{xxxx} - 2\rho_f (\partial_t + U \partial_x) \int_0^l \phi(x, 0^+, z) dz, \quad [22]$$

where we have used the linearized Bernoulli equation to determine the pressure. The last term in Eq. 22 simplifies when the flag is infinitely wide, i.e., when  $\phi(x, 0^+, z) = \phi(x, 0^+)$ . More generally, we define the function  $A(r)$

$$\int_0^l \phi_{nc}(x, 0^+, z) dz = l A(r) \phi_{nc}(x), \quad [23]$$

where  $r = (l/L)$  is the aspect ratio of the flag, and  $\phi_{nc}(x, 0^+)$  is the noncirculatory potential corresponding to the infinitely wide flag.  $A(r)$  characterizes the importance of the third dimension, and we expect that  $A(r)/r \rightarrow 1$  when  $r \rightarrow 0$  and  $A(r) \rightarrow 1$  when  $r \rightarrow \infty$ . Indeed, using a commercially available software program FEMLAB, to compute  $\phi_{nc}$  at  $y = 0^+$  as a function of  $r$  confirms this, as shown in Fig. 5. Similarly, since the circulatory potential computed via the Kutta condition (Eq. 8) is also proportional to  $A(r)$  so that Eq. 22 reads

$$(1 + A(r)\rho)\eta_{\tau\tau} = -\eta_{ssss} - \rho A(r)u_0 C[\gamma]f(s)(\eta_\tau + u_0\eta_s). \quad [24]$$

We see that including three dimensional effects modify the added mass parameter and the pressure, both of which are rescaled by a factor  $A(r)$ , which is smaller than unity. As a consequence, the marginal stability curve shown in Fig. 3 is shifted up, as shown in Fig. 3, and is even closer to the experimental data. Of course, this simple model ignores the additional complexity of vorticity distributions along the edges of

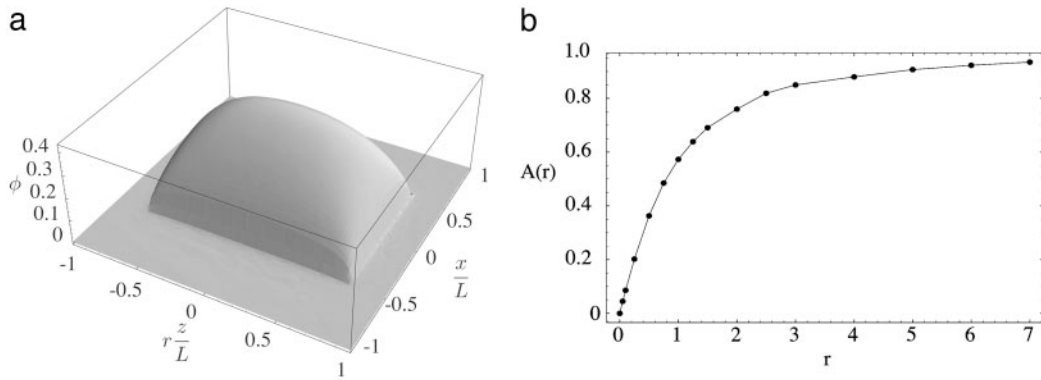


Fig. 5. Three-dimensional effects. (a) Plot of the noncirculatory velocity potential for an aspect ratio of the flag  $r = l/L = 1.5$ . (b) Plot of the aspect ratio function  $A(r)$  as function of  $r$ .

the flag, at  $z = 0, l$ , and is thus only suggestive of the general trend.

### Appendix 2: Tension Induced by the Boundary Layer

In high Reynolds number flows past the flag, the viscous boundary layer exerts a shear stress on the flag that puts it under a variable tension  $T$  which stretches the flag nonuniformly, being largest at the clamped anchor and vanishing at the trailing edge. This stabilizes the flag to some extent; in particular, it may be responsible for the experimentally observed subcritical nature of the instability (6). Restricting ourselves here to the case of the linearized theory for a slightly deformed flag with a Blasius boundary layer leads to a wall shear stress  $\tau \sim l\rho_f \sqrt{(\nu U^3/x)}$  (12), where  $\nu$  is the kinematic viscosity of the fluid. When combined with the equation for the balance of horizontal forces  $T_x = -\tau$  and the boundary condition  $T(L) = 0$ , we find that

$$T = \frac{4}{3} \frac{l\rho_f U^2}{\sqrt{Re}} \left( 1 - \sqrt{\frac{x}{L}} \right), \quad [25]$$

where the characteristic Reynolds number is defined as  $Re = UL/\nu \gg 1$ . Using this simple relation in Eq. 1 yields an eigenvalue problem similar to 21 for the instability threshold. Solving this with  $Re \sim 10^4$  shifts the marginal stability curve upwards in the direction of the experimentally obtained one, as shown in Fig. 3, but the effect is small.

This work was begun and brought to fruition when we were at Cambridge University; we dedicate this paper to the memory of Professor David G. Crighton, who first interested one of us (L.M.) in this problem nearly a decade ago. We thank M. Shelley, N. Vandenburgh, and J. Zhang for sharing their preprint with us. This work was supported by the European Community through Marie-Curie Fellowship HPMF-2002-01915 (to M.A.) and the U.S. Office of Naval Research through a Young Investigator Award (to L.M.).

1. Paidoussis, M. P. (1998) *Fluid-Structure Interaction: Slender and Axial Flow* (Academic, London).
2. Lord Rayleigh (1879) *Proc. Lond. Math. Soc.* **X**, 4–13.
3. Theodorsen, T. (1935) NACA Report 496, <http://naca.larc.nasa.gov/reports/1935/naca-report-496>.
4. von Karman, T. & Burger, J. M. (1935) in *Aerodynamic Theory*, ed. Durand, W. F. (Springer, Berlin), vol. 2.
5. Glauert, H. (1997) *Elements of Aerofoil and Airscrew Theory* (Cambridge Univ. Press, Cambridge, U.K.), 2nd Ed.
6. Zhang, J., Childress, S., Libchaber, A. & Shelley, M. (2000) *Nature* **408**, 835.
7. Watanabe, Y., Suzuki, S., Sugihara, M. & Sueoka, Y. (2002) *J. Fluids Struct.* **16**, 529.
8. Fitt, A. D. & Pope, M. P. (2001) *J. Eng. Math* **40**, 227.
9. Zhu, L. & Peskin, C. S. (2002) *J. Comp. Phys.* **179**, 452.
10. Landau, L. D. & Lifshitz, E. M. (1987) *Theory of Elasticity* (Pergamon, New York).
11. Milne-Thompson, L. M. (1960) *Theoretical Hydrodynamics* (Macmillan, New York).
12. Landau, L. D. & Lifshitz, E. M. (1987) *Fluid Mechanics* (Pergamon, New York).
13. Crighton, D. G. & Oswell, J. (1991) *Philos. Trans. R. Soc. London A* **335**, 557.
14. Lighthill, J. (1975) *Mathematical Biofluidynamics* (Soc. Indust. Appl. Math., Philadelphia).
15. Fung, Y. C. (1969) *An Introduction to the Theory of Aeroelasticity* (Dover Phoenix Editions, Mineola, NY).
16. Doedel, E. J. (2001) AUTO 2000, <http://sourceforge.net/projects/auto2000>.
17. Marsden, J. E. & Ratiu, T. S. (1994) *Introduction to Mechanics and Symmetry* (Springer, New York).